Science Advances
AAAS

advances.sciencemag.org/cgi/content/full/6/45/eabc1251/DC1

Supplementary Materials for

The 3.2-Å resolution structure of human mTORC2

Alain Scaiola, Francesca Mangia, Stefan Imseng, Daniel Boehringer, Karolin Berneiser, Mitsugu Shimobayashi, Edward Stuttfeld, Michael N. Hall, Nenad Ban*, Timm Maier*

*Corresponding author. Email: ban@mol.biol.ethz.ch (N.B.); timm.maier@unibas.ch (T.M.)

Published 6 November 2020, *Sci. Adv.* **6**, eabc1251 (2020)
DOI: 10.1126/sciadv.abc1251

The PDF file includes:

Other Supplementary Material for this manuscript includes the following:

(available at advances.sciencemag.org/cgi/content/full/6/45/eabc1251/DC1)

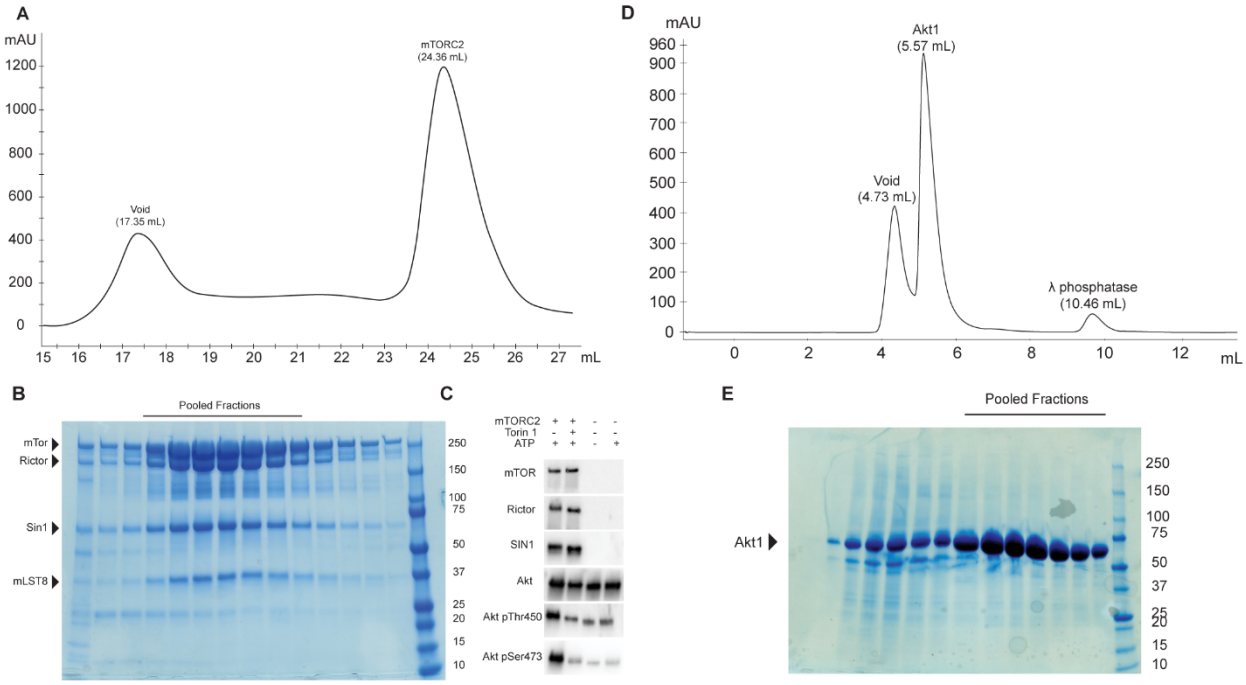

Figure S1.

mTORC2 purification and characterization and purification of Akt1. (**A**) Size exclusion elution profile of mTORC2 from a custom made Superose 6 Increase 10/600 GL column at a flow rate of 0.1 mL/min. The void and the mTORC2 peaks are indicated. (**B**) SDS-polyacrylamide gel of the fractions of the size exclusion chromatography. Fractions pooled for further analysis are indicated. Contaminant bands partially depleted in SEC chromatography have previously been identified as tubulin (apparent MW 50kD) and a viral envelope protein (25kDa) *(22)*, weak diffuse staining below the Rictor and mTOR bands results from nicking of these proteins. (**C**) Kinase activity assay of purified mTORC2 using Akt1 as a substrate. Western blots showing the phosphorylation state of Akt1 in the presence and absence of mTOR inhibitor Torin1, ATP and mTORC2. Akt1 phosphorylation is detected by phospho-specific antibodies as described in Methods. (**D**) Elution profile of Akt1 after dephosphorylation by λ-phosphatase in size exclusion chromatography on Superdex 75 Increase. The void, the Akt1 and λ-phosphatase peaks are

indicated. (**E**) SDS-polyacrylamide gel of the fractions of the size exclusion elution. Fractions pooled for the final sample are indicated.

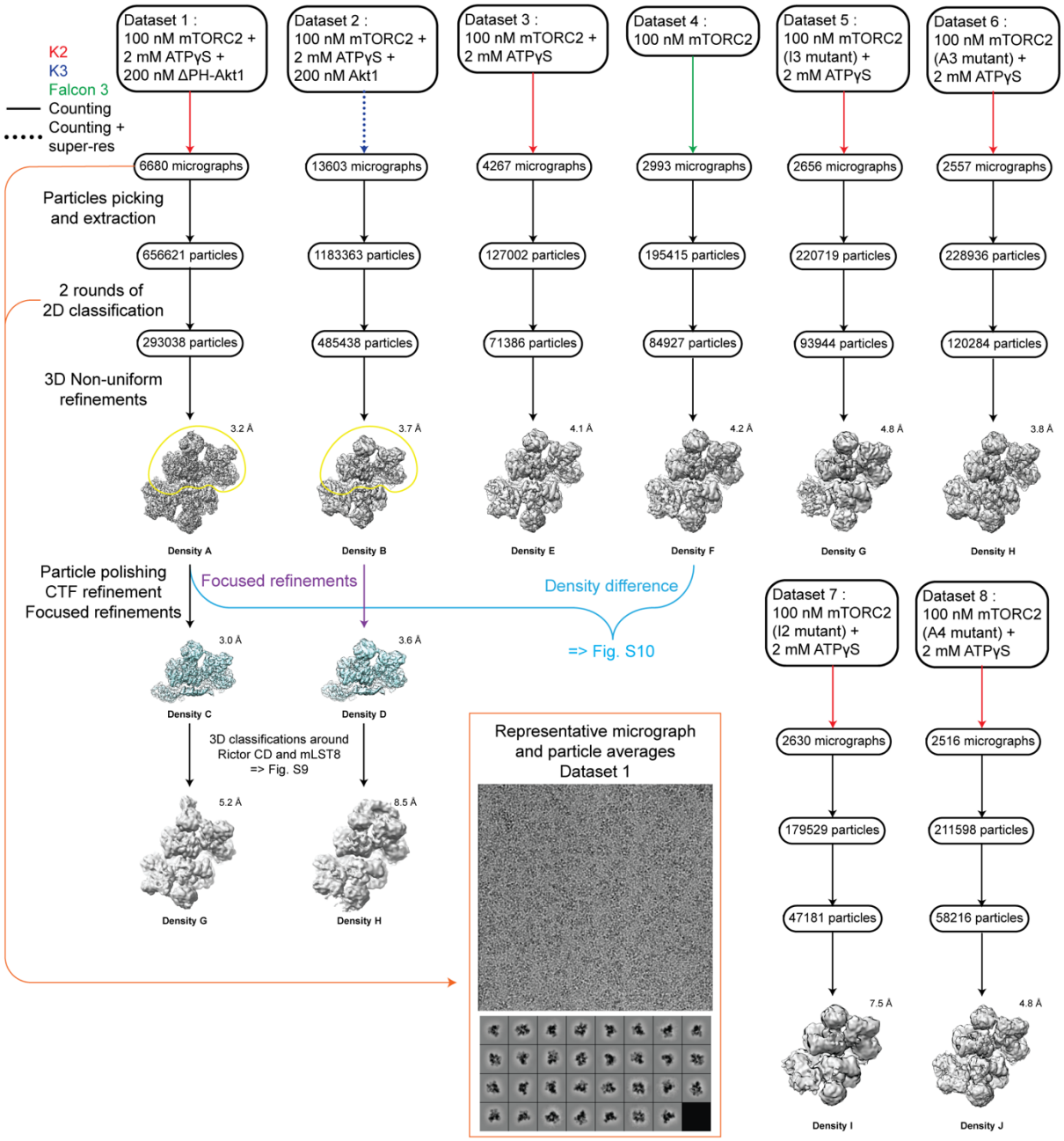

Figure S2.

Cryo-EM data processing scheme. Four datasets were collected with different conditions: with full-length Akt1 (dataset 2), ΔPH-Akt1 (dataset 1) and without Akt1 (dataset 3) in the presence of ATPγS, and dataset 4 without addition of ATPγS. Dataset 1 reached the highest resolution and was used for further processing using CTF parameter refinement and Bayesian particle polishing to

reach the highest resolution of this study, Density C, with a resolution of 3.0Å. Both datasets 1 and 2 were used for 3D classifications in the proximity of mLST8 after a refinement focused on the better half. Four further datasets (datasets 5-8) were collected for mTORC2 containing mutant variants of mTOR and Rictor, respectively, to analyze the impact of mutations. A representative micrograph, low-pass filtered at 20Å, and 2D class averages for dataset 1 are shown.

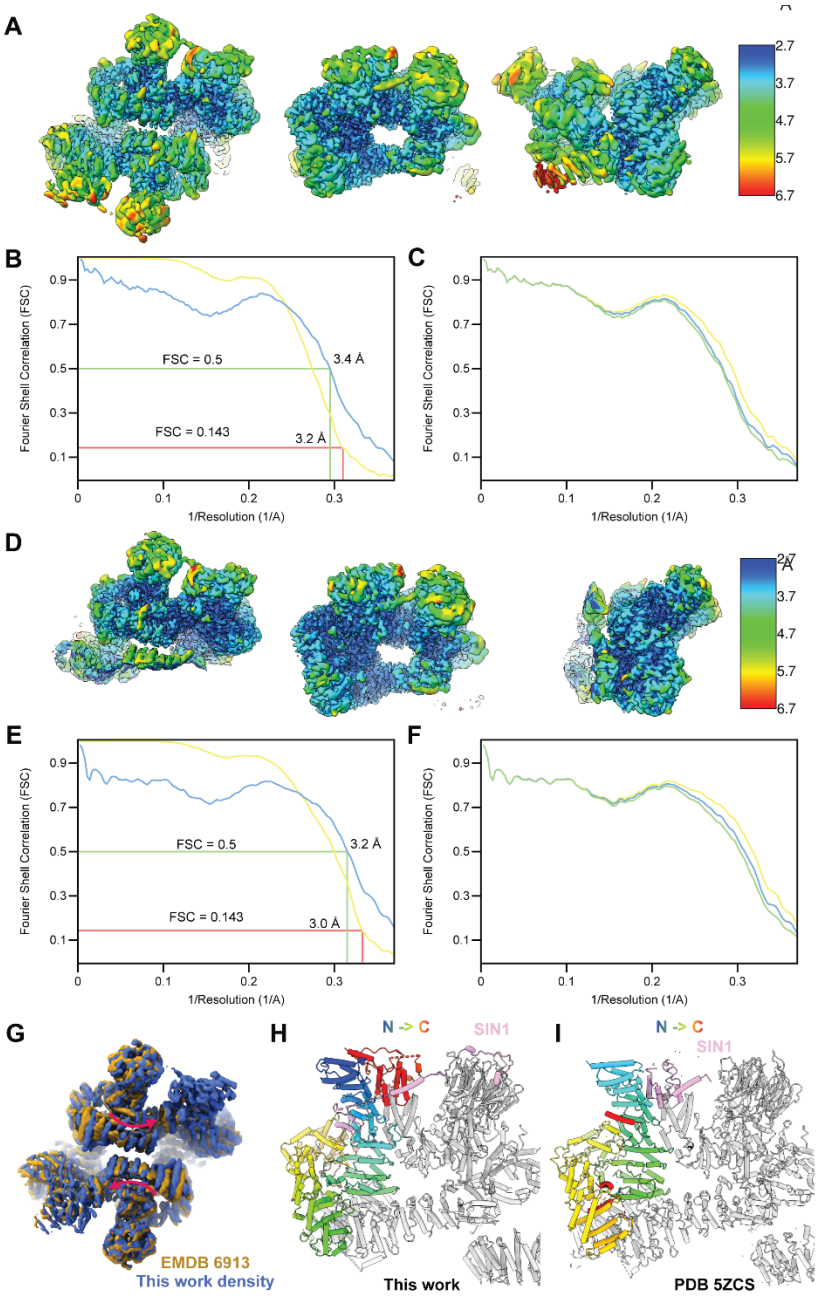

Figure S3.

Resolution of mTORC2 reconstructions and comparison to previous mTORC2 structure. (**A**) Three views of local resolution heatmaps for non-uniform refinement (Density A). Local resolution varies between ~2.7 Å in the core of one half and 6-7 Å for the flexible region of the second half. (**B**) FSC curves calculated between the two half maps (yellow) and between the model

and the non-uniform refinement map (blue). The overall resolution of the map is 3.2 Å (FSC=0.143) and is close to the 3.4 Å resolution of model versus map (FSC=0.5). The large local resolution differences (Panel A) are most likely responsible for the deviation between half-map and model-based resolution. (**C**) FSC curves calculated between the model refined in the half map 1 versus the half map 1 (blue), the half map 2 (green), and the full map (yellow). (**D**) Same as panel **A** but for the good half (Density C), which was used for model building and refinement. (**E**) and (**F**) similar to **B** and **C** respectively, but for maps calculated with a mask around the good half. (**G**) Overlay of mTORC2 density A (blue) filtered down to 4.9 Å to match the resolution of an earlier mTORC2 reconstruction (EMDB 6913 *(20)*) showing the inward rotation of the FAT region in the current reconstruction. A similar mode of rotation is apparent when comparing to an earlier intermediate resolution structure of human mTORC2 (EMDB 3927 *(22)*). (**H**) and (**I**), Overview of Rictor and SIN1 topology in the current structure (**H**) and a previous mTORC2 model (PDB: 5ZCS *(20)*) (**I**). SIN1 is coloured in pink and Rictor is coloured by sequence from blue (N-terminus) to red (C-terminus).

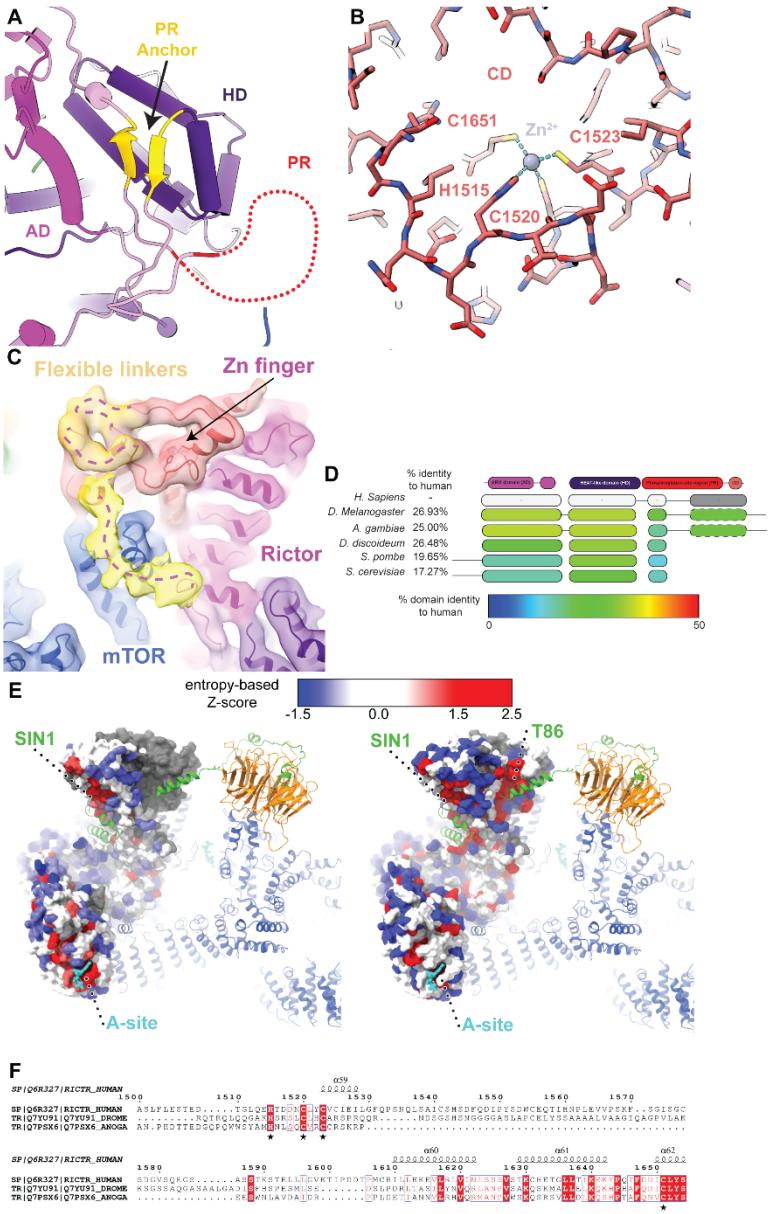

Figure S4.

PR anchor and Zn^{2+} binding site in Rictor. (**A**) Close-up view of the antiparallel-strands (gold) which are located in sequence before and after the PR of Rictor, anchoring the PR to the top of HD. (**B**) Close-up view of the Rictor CD zinc finger, which is part of the four-helix bundle and is formed by His1515, Cys1520, Cys1523, and Cys1651. (**C**) An overall mTORC2 reconstruction filtered to 6Å resolution reveals flexible linker segments (dashed line) and the connectivity in the

CD region. The map is shown at 4σ contour level and flexible linkers are highlighted in orange (3.5σ contour level). Another linker visible at lower contour level (shown at 2.5σ contour level in yellow) shows the connectivity to the preceding structured segment of Rictor. (**D**) Sequence conservation in Rictor. A multiple sequence alignment of Rictor orthologs is analysed by AL2CO *(62)* (entropy based conservation measure, independent counts) which shows four conserved blocks colored according to their respective percent identity relative to *H. sapiens* Rictor. The fourth block, corresponding to the end of the PR and the CD, is only conserved in metazoans. (**E**) Surface representation of Rictor coloured by residue conservation within eukaryotes (left) and metazoans (right). Blue represents poorly conserved residue, while red shows high conservation. Conserved patches are found around the A-site and the region interacting with SIN1. Grey regions are not found in all species compared. (**F**) Multiple sequence alignment of metazoan homologs of Rictor around the Zinc finger. The residues coordinating the zinc are underlined with a star.

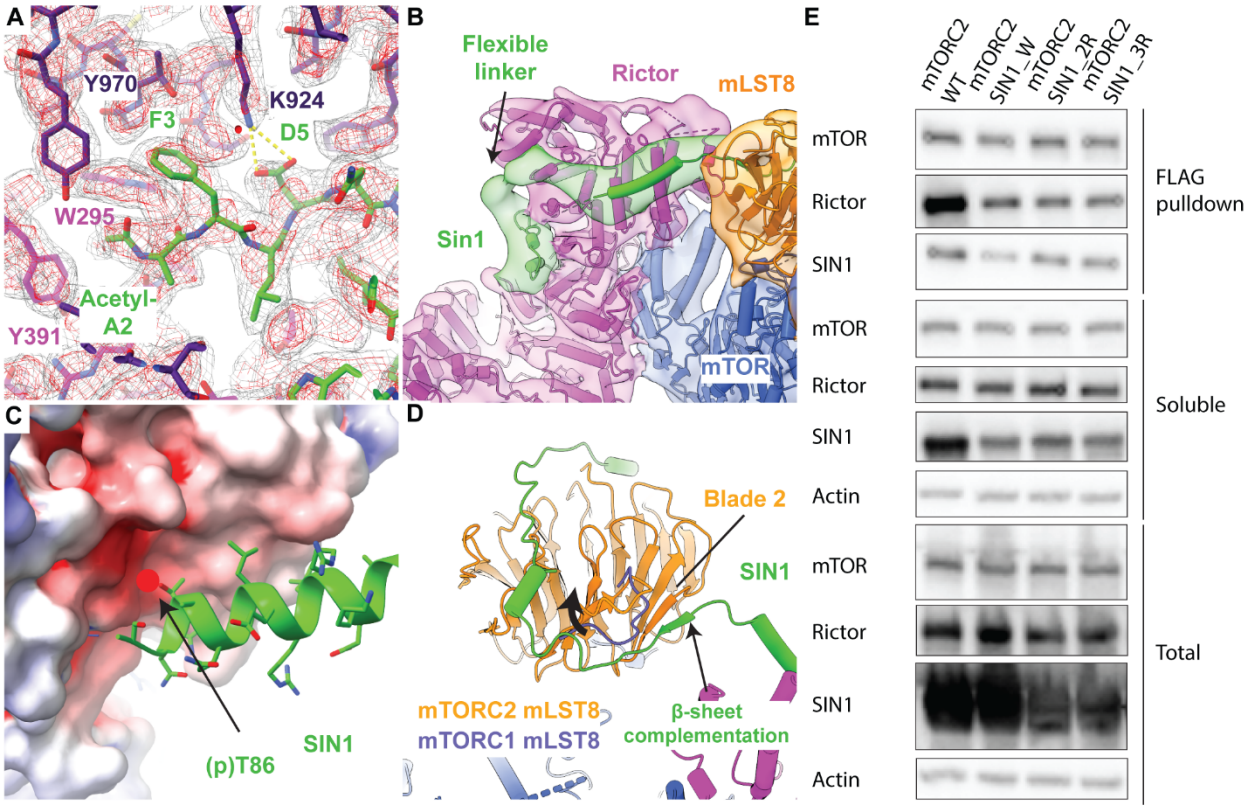

Figure S5.

Features and interactions of SIN1. (**A**) Close-up view of the N-terminal region of SIN1 (green), which is found deeply inserted between the AD (magenta) and the HD (dark magenta) of Rictor. Possible hydrogen bonds are indicated as a dashed yellow line. (**B**) Overview of the poorly ordered SIN1 linker between its N-terminal region and the traverse shown using a map filtered to 10Å resolution. (**C**) Close-up view of Thr86 of SIN1. Rictor is shown as a surface and coloured according to the electrostatic potential. Thr86 is inserted into a negatively charged pocket and phosphorylation (red circle) is likely incompatible with insertion into this pocket. (**D**) Different conformations of the linker between sheet three and four of the third blade of mLST8 are observed in mTORC2 (orange) and mTORC1 (blue). SIN1 extends towards the second blade of mLST8 and interacts via β-strand complementation. (**E**) Analysis of expression and mTORC2 integration of

SIN1 variants. Western blot from lysate and mTOR-based FLAG-bead pulldown of insect cells recombinantly overexpressed mTORC2 WT and mTORC2 carrying variants of SIN1 with insertion of a tryptophan (mTORC2 SIN1_W), two consecutive arginines (mTORC2 SIN1_2R) and three consecutive arginines (mTORC2 SIN1_3R) at its processed N-terminus. Total lysate, soluble input protein after centrifugation and Flag-bead pulldown were blotted with immunodetection for mTOR, Rictor and SIN1. Actin was used as loading control. mTOR, Rictor and SIN1 expression levels are comparable in the WT and SIN1 N-terminal variants, but Rictor and SIN1 pull-down is lower in mutant variants than in mTORC2 WT.

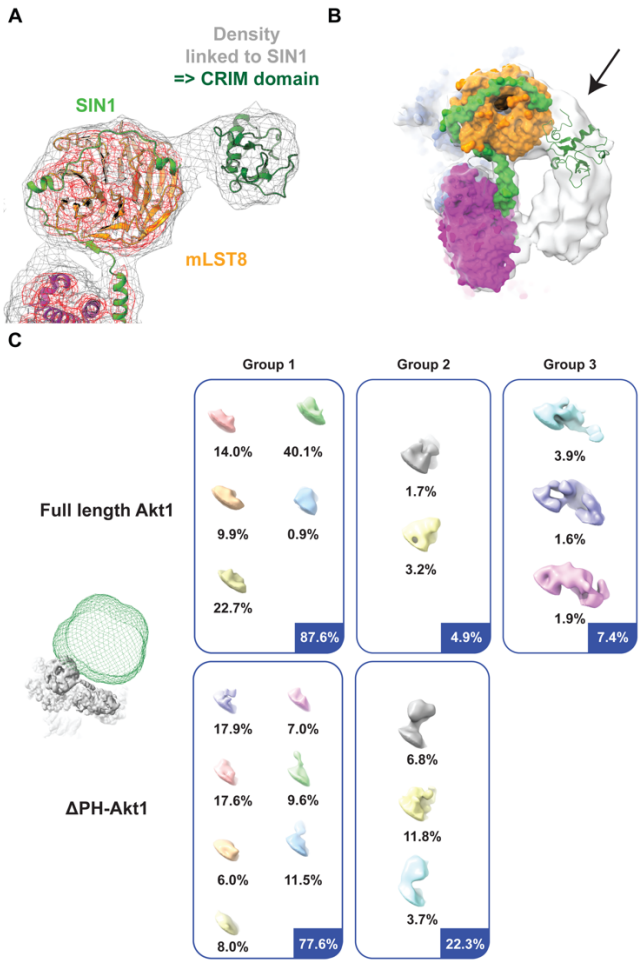

Figure S6.

Local structural features and substrate recognition by SIN1. (**A**) Overview of SIN1 and mLST8 in density G (Fig. S2), shown at two different contour levels (red and grey), highlights the extra density found in the continuation of SIN1. (**B**) View of the structure above the catalytic site shown within density H (Fig. S2) showing the visible arch of extra density found between mLST8 and Rictor. The structure of the CRIM domain (PDB 2RVK *(26)*) was fitted into the density, explaining part of the arch. The second part cannot be explained unambiguously. (**C**) Local classification without alignment around the SIN1 CRIM domain in density G (Fig. S2). Top view of 3D classes calculated with a mask around Rictor CD and mLST8 (show on the left in green

relative to the high-resolution reconstruction). The top ten classes are calculated from datasets collected for samples containing full length Akt1, while the bottom ten classes are of samples containing ΔPH-Akt1. Classes showing small extra density, probably corresponding to the CRIM domain were put in group 2, while the classes showing a more “arch”-like structure were put in the group 3.

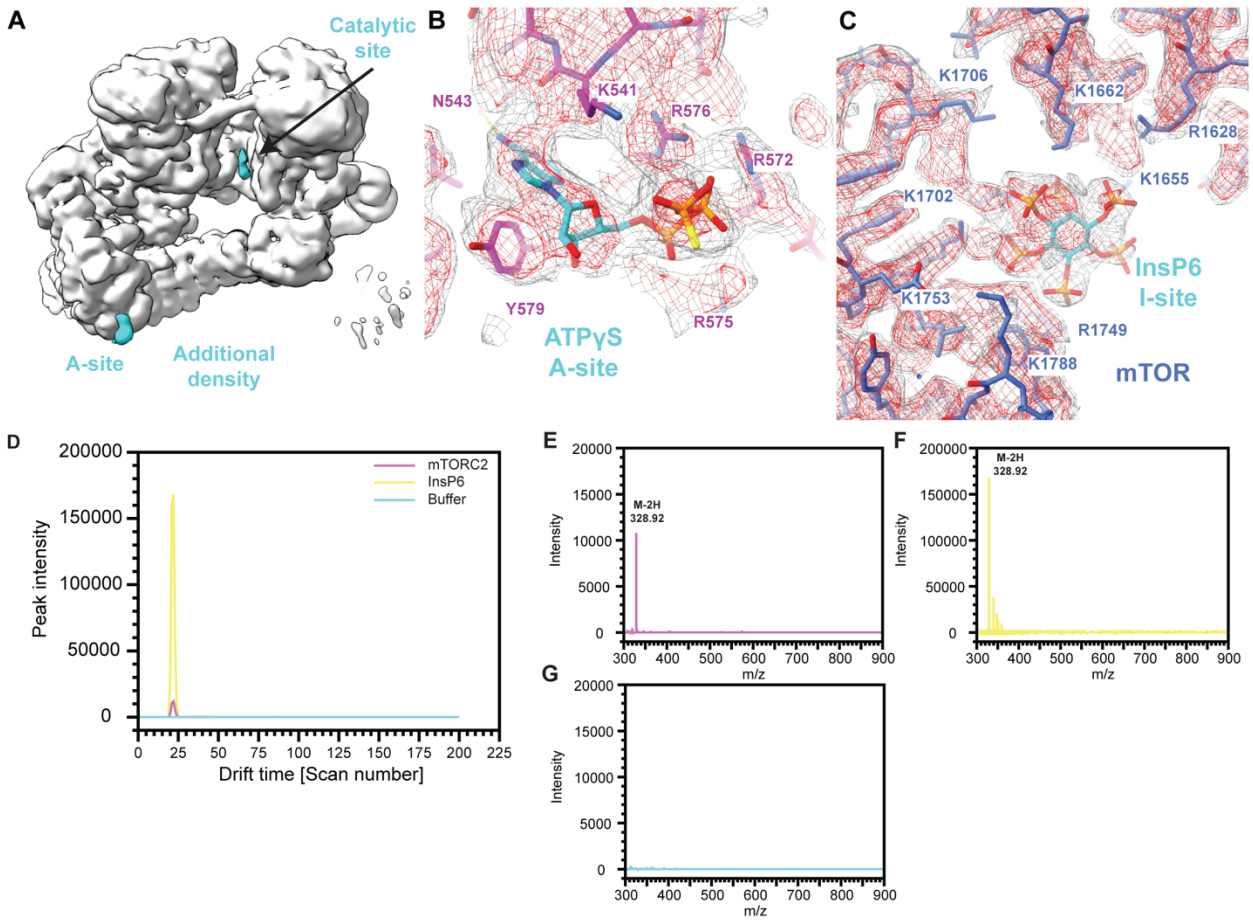

Figure S7.

mTORC2 ligand binding sites. (**A**) Difference densities between the reconstructions in presence (Density A, low pass filtered to 3.9Å) and absence of ATPγS (Density F, showed in grey) are shown in light blue (shown at 4σ) in the A-site and the catalytic site, highlighting the similarity of differences in both site (**B**) Close-up view of ATPγS in the A-site in Rictor. (**C**) Close-up view of InsP6 bound to the I-site in the FAT domain of mTOR (blue). For panel (**B**), and (**C**), density for the focused refinement around one protomer (Density C) is shown in mesh style at two contour levels (grey and red). (**D**)-(**G**) Mass spectrometry analysis for ligand identification. (**D**) Ion mobility chromatogram for m/z 328.92 +/- 0.01 Da. The buffer control curve (blue), which was treated as the sample one (magenta) does not show any peak in this range, while the InsP6 reference

(yellow) shows a strong peak around scan 22. The same peak was found in our sample (magenta) at the same drift time. (**E-G**) Mass spectra corresponding to the scan 22 in the ion mobility are shown between 300 and 900 Da. Peaks corresponding to the doubly charged InsP6 are observable in the mTORC2 sample (magenta) (E) and in the InsP6 reference sample (yellow) (F); no significant peaks are detected in the buffer control (G).

Figure S8.

Sequence conservation of Rictor. Multiple sequence alignment of Rictor orthologs showing conservation and secondary structure. Blue boxes represent region of BLOSUM62 similarity score above 0.1, while the one highlighted in red are strictly conserved among the shown sequences.

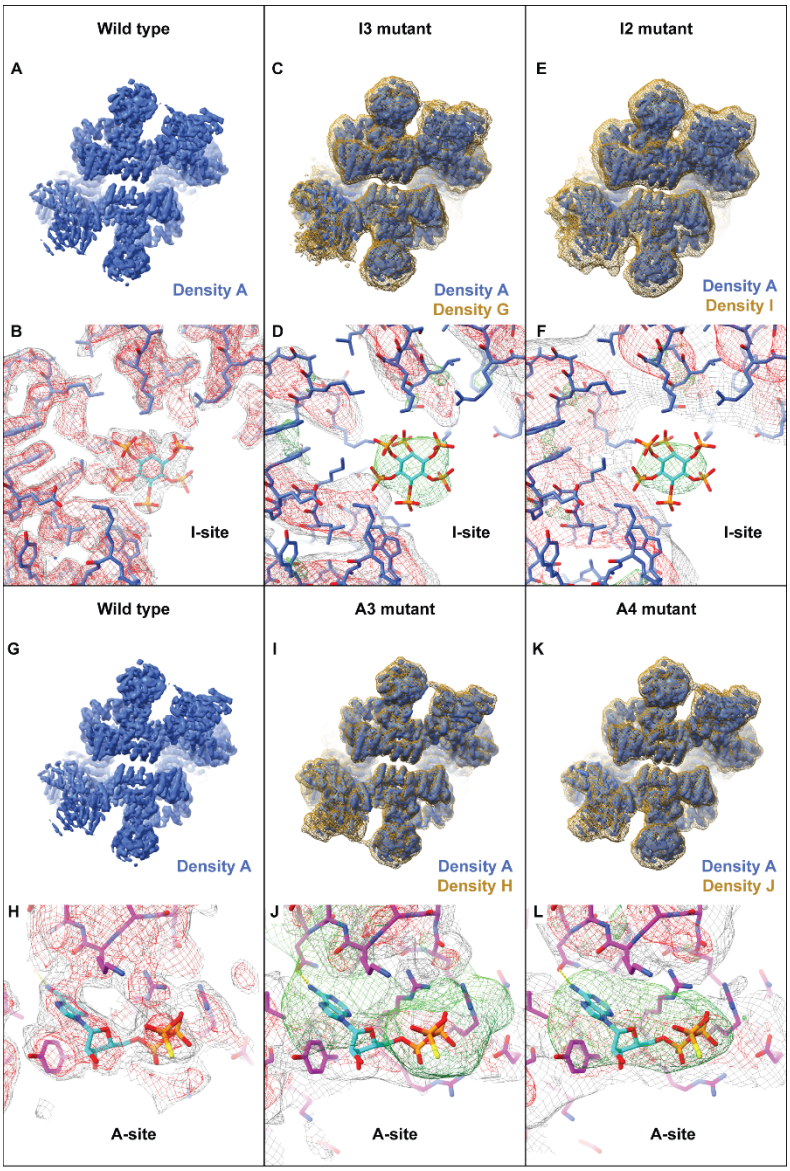

Figure S9.

Comparison of reconstructions of wild type mTORC2 and I-site or A-site variants. (**A**) and (**G**): Overall cryoEM reconstruction of wt-mTORC2 in presence of ATPγS and ΔPH-Akt1 for the indicated variants of mTORC2. (**B**). Close-up view of the I-site in the wt-mTORC2. (**C**), (**E**), (**I**), and (**K**) Overlay of mTORC2 density A (blue) filtered down to 4.9 Å with mutant mTORC2 reconstruction. (**D**),(**F**). Close up-view of the I-site of the mTOR mutants (grey and red) with the difference density with the wt-mTORC2 (green). (**H**) Close-up view of the A-site in the wt-

mTORC2. (**J**),(**L**). Close up-view of the A-site of the mutant Rictor mutant (grey and red) with the difference density with the wt-mTORC2 (green).

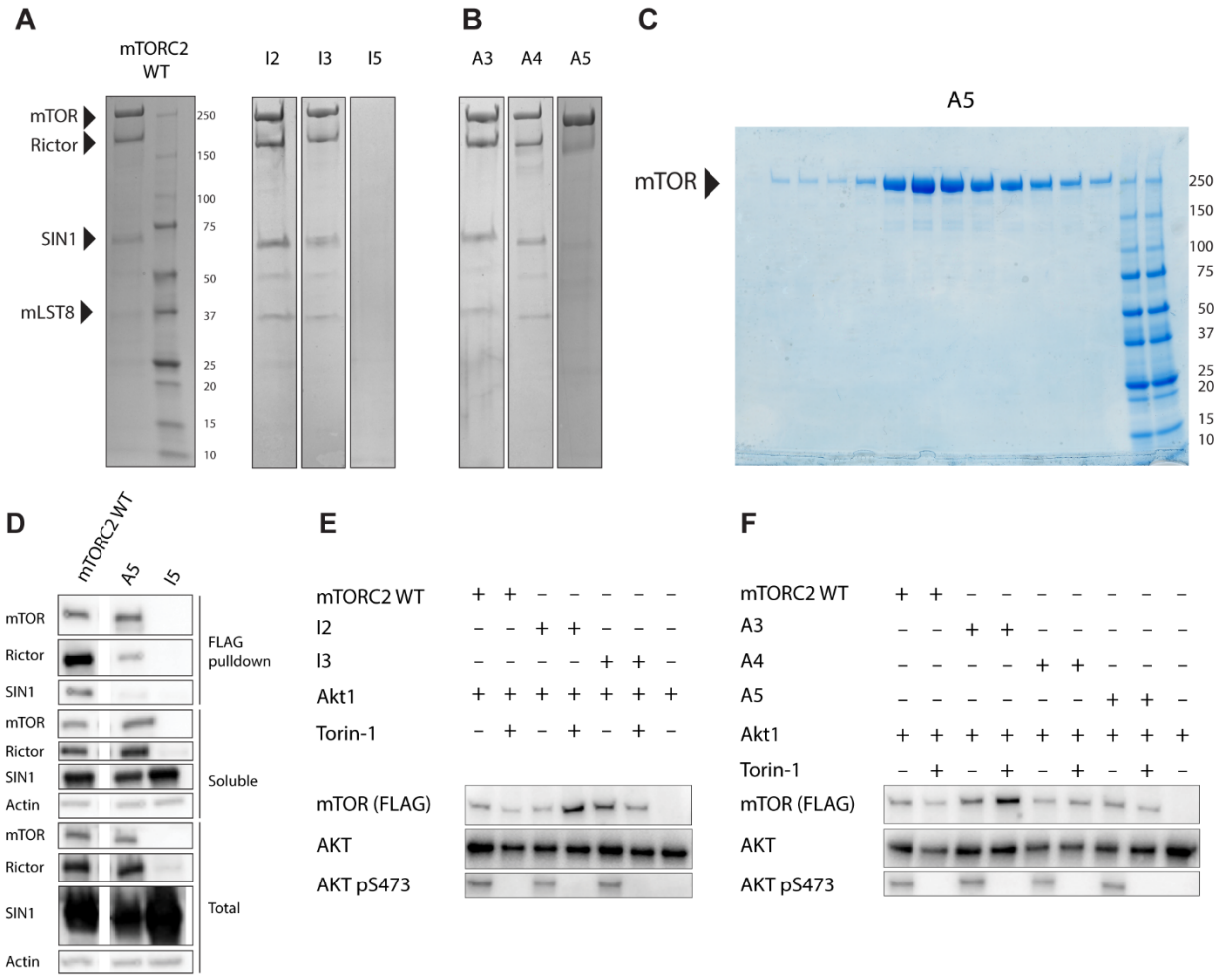

G

	Apparent Melting Point °C		
Sample ID	Mean	SD	Replicates
mTORC2 WT	44.7	0.428	5
I2	42.8****	0.354	5
I3	44.4	0.339	5
A3	44.0	0.563	5
A4	43.6**	0.443	4
A5	Not measurable		

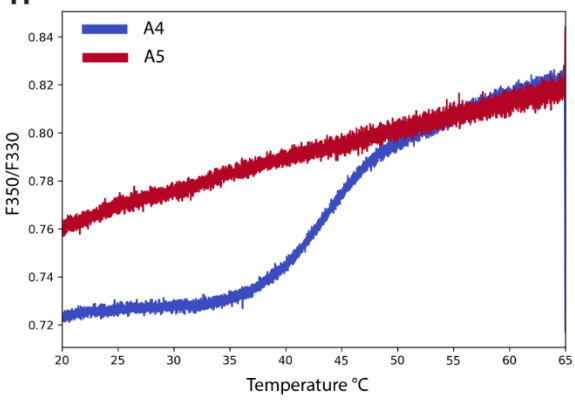

Figure S10.

Biochemical analysis of A- and I- site mutants of mTORC2. (**A**)-(**D**) Expression and assembly of A- and I- site mutants into mTORC2. (**A**) Coomassie-stained SDS-polyacrylamide gel analysis of mTOR-based FLAG bead pulldown from recombinant overexpression in insect cells for mTORC2 WT and three variants with mutations in the I-site. mTOR mutants I2 and I3 assemble into mTORC2 complexes, for mutant I5, neither mTOR nor other mTORC2 subunits are pulled down. (**B**) Coomassie-stained SDS-polyacrylamide gel of a small-scale mTOR-based FLAG bead pulldown of three Rictor A-site mutants. Mutants A3 and A4 assemble into mTOR complexes. Mutant A5 shows lower level of pulled down Rictor and SIN1. (**C**) SDS-polyacrylamide gel of size exclusion chromatography after up-scaled recombinant insect cell overexpression of mTORC2 with Rictor variant A5. Purification yielded a diminished Rictor content, indicating defective complex assembly. (**D**) Analysis of protein levels from recombinant overexpression in insect cells of mTORC2 components for mutant variants I5 and A5, which show no or partial complex assembly. Rictor mutant A5 shows comparable expression levels to WT in the total and input fractions but less SIN1 and Rictor are pulled down, indicative of defective complex assembly. For mTOR mutant I5, mTOR is not detected, Rictor levels are lower than WT, but SIN1 is present at WT levels. **(E) - (F)** Effect of A- and I- site mutations on mTORC2 activity in vitro. In vitro kinase activity assay of purified mTORC2 for two I-site and three A-site variants (A5 purifies as only mTOR) compared to mTORC2 WT, using Akt1 as substrate and immunodetection of AKT pSer473 as readout for activity. Addition of Torin-1 is used for negative control. (**E**) Analysis of I-site variants I2 and I3, all variants display activity. (**F**) Analysis of A-site variants A3, A4 and A5 (purified with diminished Rictor content), all variants display activity. (**G**)-(**H**)

Thermal stability of A- and I- site variants of mTORC2. (**G**) Mean and SD of the mean of the melting points of mTORC2 WT and two I-site and two A-site variants, as recorded by nanoDSF measurements. Significance of difference in melting points between mutants and wild-type was analyzed by unpaired, two-sided t-test and indicated by asterisks (**: $p \leq 0.01$; ****: $p \leq 0.0001$). (**H**) Plot of the ratio of fluorescence at wavelengths 350/330 nm plotted against increasing temperature to determine the Tm of the analyzed protein. Variant A5, which purifies with diminished Rictor content shows no defined melting point, in contrast to variant A4 that contains only one mutation less, indicating exposure of tryptophan residues already at low temperatures.

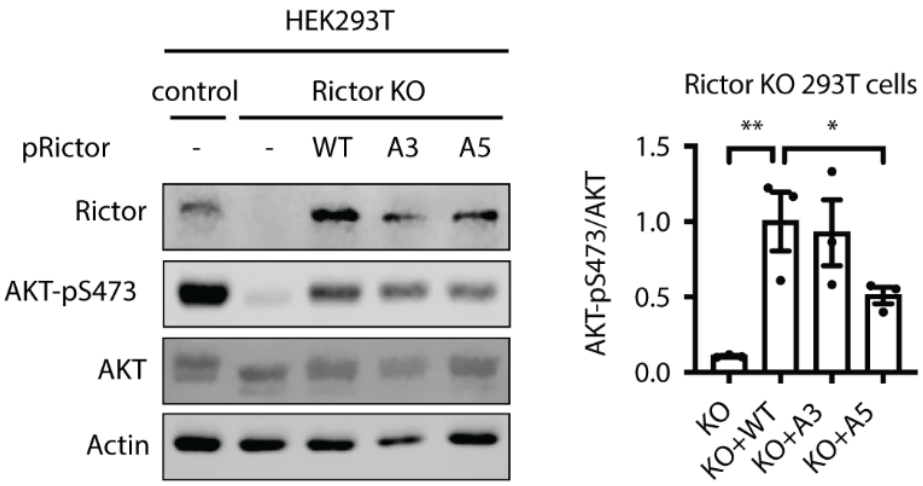

Figure S11.

In cell mTORC2 activity for mTORC2 A-site variants. Immunoblots of lysates from control or Rictor knockout HEK293T cells complemented with Rictor-WT, Rictor variant A3, or Rictor variant A5. Cells were starved for serum for overnight and stimulated with 10% FCS and 100 nM insulin for 15 min. Actin serves as a loading control. For quantification, AKT-pS473 signals are normalized to total AKT signals. One-way ANOVA, **$p<0.01$, *$p<0.05$. N=3.

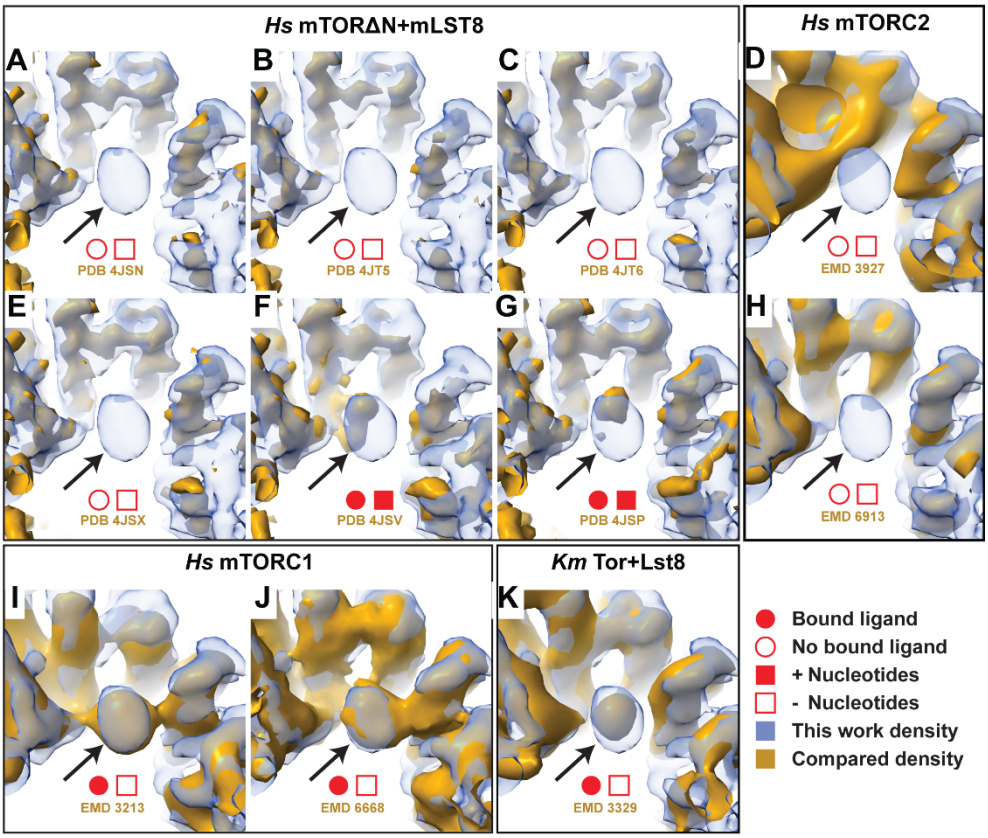

Figure S12.

Comparison of the I-site in published structures of mTOR complexes. Close up view of the I-site (arrow) in the mTORC2 density (blue mesh) compared with published density maps (dark yellow). (**A-C**) and (**E-G**). Densities for crystal structures of human mTOR-mLST8. Extra density can be seen in the I-site in densities corresponding to PDB 4JSV *(27)* and 4JSP *(27)* panel F and G. These structures were obtained in presence of ATP analogs. (**A,B,C** and **E**) structures were obtained in absence of ATP or ATP analogs. (**D** and **H**), Comparison to human mTORC2 from EMD 3927 *(22)* and EMD 6913 *(20)* in which no ligand binding is observed. (**I-K**) Densities from low and medium resolution cryoEM reconstructions which also show extra density in the I-site. The densities come from (**I**) human mTORC1 (EMD 3213 *(16)*) and from (**J**) human mTORC1(EMD 6668) and from (**K**) fungal Tor-Lst8 (EMD 3329 *(19)*). (**I-K**) Densities were

obtained in absence of ATP analogs. Together these results suggest that InsP6 can be copurified presumably depending on cellular InsP6 concentration and specific purification conditions. Appearance of density in the I-site upon nucleotide analogue supplementation suggests the possibility of alternate binding of nucleotides to the mTOR I-site, when it is not occupied by Ins6P.

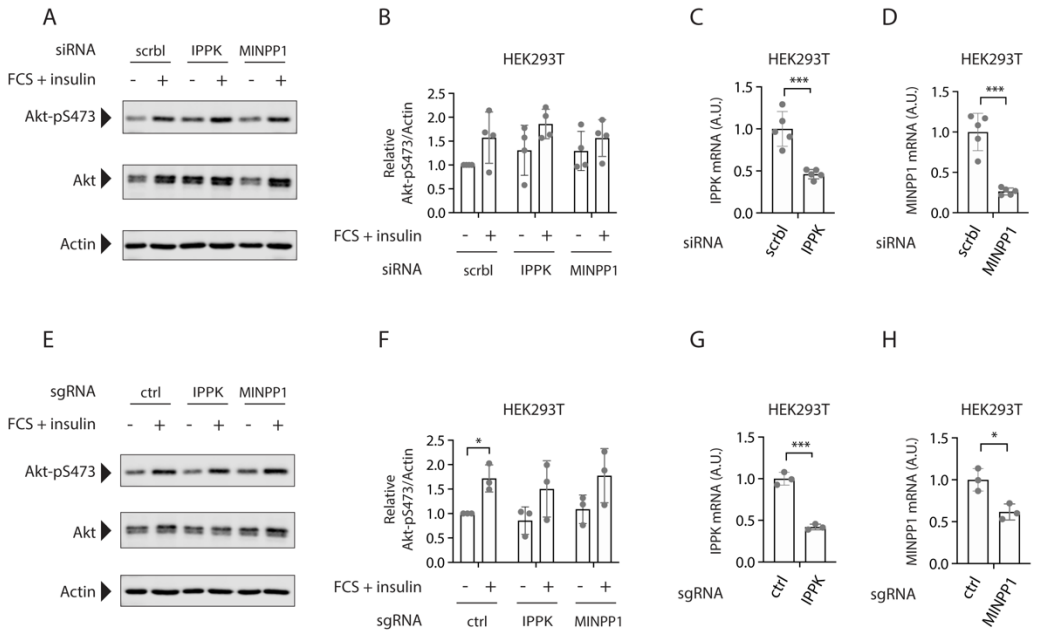

Figure S13.

Knock-down or knock-out of IPPK or MINPP1 does not alter mTOR-Akt signalling (**A**) Western Blot showing Akt phosphorylation under starving and stimulating conditions. IPPK and MINPP1 knockdown cells were generated using HEK293T cells. n=3 (**B**) Quantification of western blot in A) and all biological replicates (n=3). (**C,D**) Knockdown validation via qRT-PCR analysis of IPPK and MINPP1 knockdown cells (n=5). (**E**) Western Blot showing Akt phosphorylation under starving and stimulating conditions. IPPK and MINPP1 knockout cells were generated using HEK293T cells. n=2. (**F**) Quantification of western blot in D) and all biological replicates (n=2). (**G,H**) Knockout validation via qRT-PCR analysis of IPPK and MINPP1 knockouts in HEK293T cells (n=2). Sequencing results of PCR fragments including the sgRNA binding site were interrupted, which suggests successful Cas9 activity and knockout of IPPK and MINPP1.

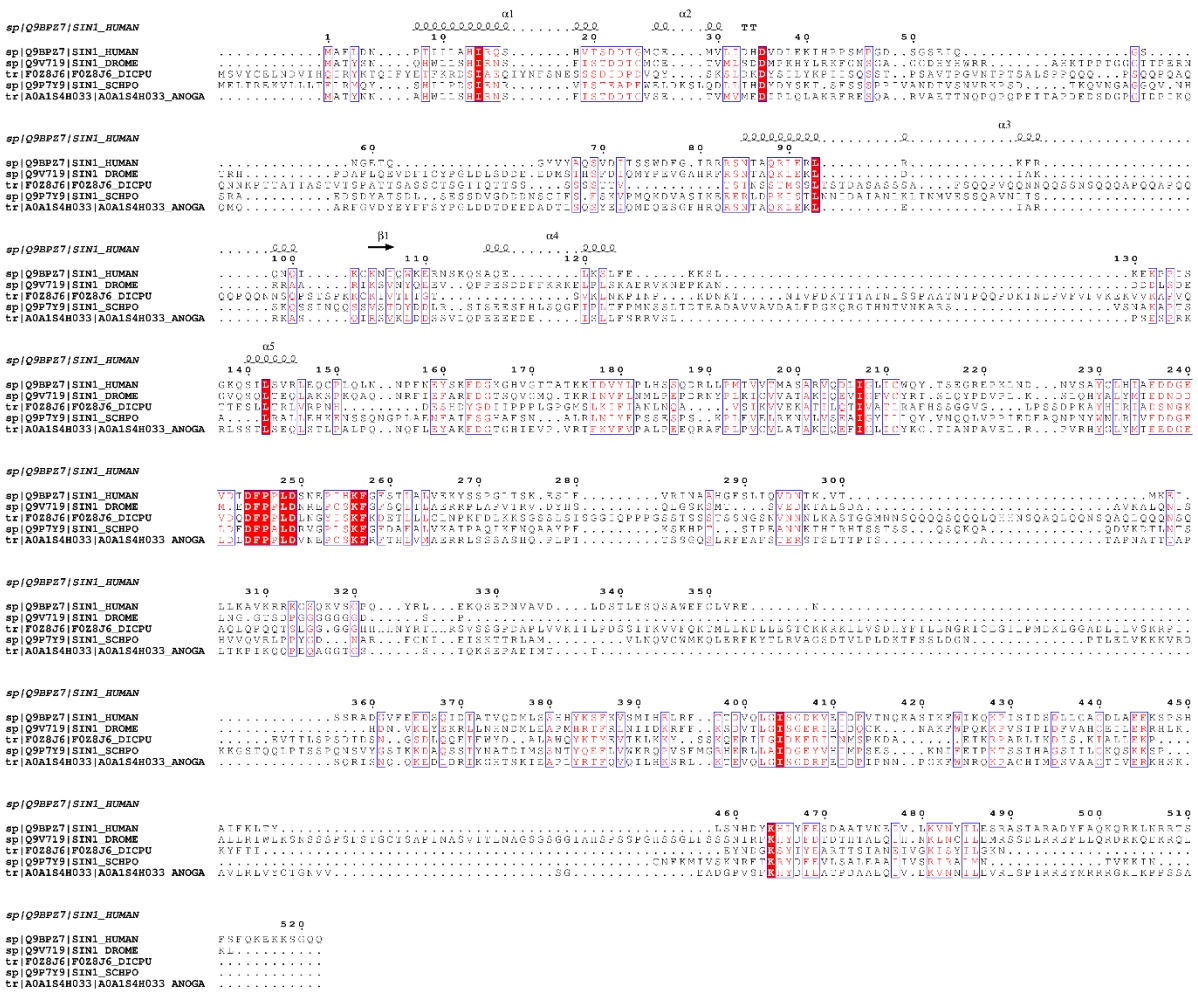

Figure S14.

Sequence conservation of SIN1. Multiple sequence alignments of SIN1 homologs showing conservation and secondary structure. The sequence of the *S. cerevisiae* SIN1-homolog Avo1 was omitted for clarity as it contains several large insertions.

Table S1.

Generation of variants of mTORC components.

ID	Mutant type	Mutations	Primers
I2	I- site double mutant	mTOR_K1753E_K1788E	Forward: GAGCTTGGAGAGTGGCAGCTGAATCTACA GGGCATCAATGAGAGCACAATCCCCAAAG TGCTGCAGTACTACAGCGCCGCCACAGA GCACGACCGCAGCTGGTACGAGGCCTGG CATG Reverse: CAGGAAGCATCGGGCCATGAGCTTGTGCA GTTCCTGCTTA
I3	I- site triple mutant	mTOR_R1628E_K1655E_K1662E	Forward: GAGATCGTAGAGGACTGGCAGAAAATCCT TATGGTGCGGTCCCTTGTGGTCAGCCCTC ATGAAGACATGAGAACCTGGCTCGAGTAT GCAAGCCTGTGCGGCGAGAGTGGCAGGC TGG Reverse: CTGGCAGCCCTGCAGTCTCTCCCACCAGA T
I5	I- site quintuple mutant	mTOR_R1628E_K1655E_K1662E _K1706E_K1735E	Restriction and ligation of synthetic DNA fragment
A3	A- site triple mutant	Rictor_R572E_R575E_R576E	Forward: GAGTTTGTAGAGGAGCTACTTTATTTTTAC AAGCCCAGCAGTA Reverse: GTGTAACTGTTCATCTTTATAGTTTCTTAG
A4	A- site quadruple mutant	Rictor_R572E_R575E_R576E _Y579A	Forward: GAGTTTGTAGAGGAGCTACTTGCATTTTAC AAGCCCAGCAGTAAATTATAT Reverse: GTGTAACTGTTCATCTTTATAGTTTCTTAG
A5	A- site quintuple mutant	Rictor_R572E_R575E_R576E _Y579A_L587W	Forward: GAGTTTGTAGAGGAGCTACTTGCATTTTAC AAGCCCAGCAGTAAATGGTATGCCAACCT GGAT Reverse: GTGTAACTGTTCATCTTTATAGTTTCTTAG
mTORC2 SIN1_W	SIN1 N-terminal extension	SIN1 N-terminal extension of one Tryptophan	Forward: TGGGCCTTCTTGGACAATCCAACTATCAT Reverse: CATGGTGGCGGTTTTTTATAAG
mTORC2 SIN1_2R	SIN1 N-terminal extension	SIN1 N-terminal extension of two Arginines	Forward: CGACGAGCCTTCTTGGACAATCCAACTAT CATTCTAGC Reverse: CATGGTGGCGGTTTTTTATAAG
mTORC2 SIN1_3R	SIN1 N-terminal extension	SIN1 N-terminal extension of three Arginines	Forward: CGACGACGAGCCTTCTTGGACAATCCAAC TATCATTCT Reverse: CATGGTGGCGGTTTTTTATAAG

Table S2.

Data collection and refinement statistics for mTORC2 half and complete complex.

	Non-uniform refinement (EMDB-11488) (PDB 6ZWM)	Focus refinement on one half (EMDB-11492) (PDB 6ZWO)
Data collection and processing		
Magnification	59500x	59500x
Voltage (kV)	300	300
Electron exposure (e–/Å^2)	~70	~70
Defocus range (μm)	1.0-3.0	1.0-3.0
Pixel size (Å)	1.34 (1.6x binned)	1.34 (1.6x binned)
Symmetry imposed	C1	C1
Initial particle images (no.)	656'621	656'621
Final particle images (no.)	293'038	293'038
Map resolution (Å)	3.2	3.0
FSC threshold	0.143	0.143
Map resolution range (Å)	2.7-~7	2.7-~7
Refinement		
Initial model used (PDB code)	5ZCS (mTOR+mLST8)	5ZCS (mTOR+mLST8)
Model resolution (Å)	3.4	3.2
FSC threshold	0.5	0.5
Model resolution range (Å)	3.2 -	3.0 -
Map sharpening *B* factor (Å^2)	97.47	69.09
Model composition		
Non-hydrogen atoms	56947	24994
Protein residues	7437	3126
Ligands	8	4
B factors (Å^2)		
Protein	122.01	42.44
Ligand	132.774	59.92
R.m.s. deviations		
Bond lengths (Å)	0.004	0.002
Bond angles (°)	0.808	0.513
Validation		
MolProbity score	1.57	1.68
Clashscore	3.83	6.22
Poor rotamers (%)	1.59	1.3
Ramachandran plot		
Favored (%)	96.30	96.29
Allowed (%)	3.68	3.71
Disallowed (%)	0.03	0.00

Movie S1.

Visualization of the first and second component of the variability analysis done in Cryosparc v2, showing the continuous motion found within the particle set.

Movie S2.

Overview of the human mTORC2 complex, followed by a close-up view of the I-site, the binding site of InsP6 common to mTORC1 and mTORC2.

Movie S3.

Overview of the domain architecture of Rictor in mTORC2. ATPγS binds the A-site in the HEAT-like domain (HD) of Rictor.

Movie S4.

Overview of SIN1 integration into mTORC2. The SIN1 N-terminus tightly interacts with Rictor. SIN1 traverses the catalytic site cleft and winds around mLST8.